



# Syngas production by methane oxy-steam reforming on Me/CeO<sub>2</sub> (Me = Rh, Pt, Ni) catalyst lined on cordierite monoliths



Antonio Vita<sup>a,\*</sup>, Giuseppe Cristiano<sup>b</sup>, Cristina Italiano<sup>a</sup>, Lidia Pino<sup>a</sup>, Stefania Specchia<sup>b</sup>

<sup>a</sup> CNR-ITAE "Nicola Giordano", Via Salita S. Lucia sopra Contesse 5, 98126 Messina, Italy

<sup>b</sup> Politecnico di Torino, Department of Applied Science and Technology, Corso Duca degli Abruzzi 24, 10129 Torino, Italy

## ARTICLE INFO

### Article history:

Received 12 April 2014

Received in revised form 7 July 2014

Accepted 11 July 2014

Available online 19 July 2014

### Keywords:

Syngas production

CH<sub>4</sub> oxy-steam reforming

Rh Pt Ni catalysts

Ceria carrier

Cordierite monoliths

## ABSTRACT

The deposition of catalytic layers as Rh, Pt, Ni (noble metals load equal to 1.5 wt.%, Ni load equal to 7.5 wt.%) on CeO<sub>2</sub>, over cordierite monoliths (400 cpsi, diameter 1 cm, length 1.5 cm), prepared through a combination of the solution combustion synthesis followed by the Wet Impregnation technique, was investigated. The performances of the structured catalysts were evaluated towards the methane Oxy-Steam Reforming (OSR) reaction. The physicochemical properties of the catalysts at powder level were investigated by X-ray Diffraction, CO chemisorption and nitrogen adsorption (BET), whereas the characteristics of the structured catalysts in terms of thickness and coating integrity were investigated by Scanning Electron Microscopy (SEM), mechanical strength and pressure drop tests. Moreover, the morphology of catalytic layers was investigated by Transmission Electron Microscopy (TEM) on the powder obtained by mechanically scraping the monoliths internal walls. The prepared structured catalysts were tested and compared towards the CH<sub>4</sub> OSR reaction varying the temperature (500–800 °C), the weight space velocity (WSV = 33,000–400,000 Nml g<sub>cat</sub><sup>−1</sup> h<sup>−1</sup>), at fixed molecular oxygen-to-carbon (O/C = 0.55) and steam-to-carbon (S/C = 1.2) molar ratios. The catalytic monoliths presented a uniform thin coating with thickness between 20 and 25 μm, high mechanical strength and low pressure drop. Regarding the catalytic activity, at low WSV all of the structured catalysts showed similar performances. Instead, increasing the WSV, the catalytic monolith loaded with 1.5 wt.% Rh/CeO<sub>2</sub> performed slightly better than the other samples, maintaining almost constant the methane conversion and the CO selectivity even at 400,000 Nml g<sub>cat</sub><sup>−1</sup> h<sup>−1</sup>.

© 2014 Elsevier B.V. All rights reserved.

## 1. Introduction

Hydrogen is, currently, one of the important gaseous raw materials for petroleum and petrochemical industries. In the near future hydrogen is expected to become an important energy carrier [1] to be used for Fuel Cells (FC) in electrical vehicles (Proton Exchange Membrane FC, PEMFC [2]) and electrical power plants (Solid Oxide FC, SOFC [3]) with zero, or near-to-zero emissions of greenhouse gases or hazardous species. This scenery is connected with a new prospective in terms of energy production, finalized to minimize or solve problems due to the global warming, the lack of fossil resources and the general increase of energy demand especially by the new emergent economies [4]. Therefore, the hydrogen demand is expected to grow over the next ten years, for industrial use, and for running FC [5].

The feasibility of a truly hydrogen economy is still an open debate: the production, transport and use of hydrogen as a fuel or raw material for other chemicals require a series of new processes, materials, products and infrastructure which necessitate resources not yet available. The introduction and commercialization of hydrogen as future energy carrier requires many efforts, also considering safety and regulations [6–8].

Thus, the interest in the use of syngas (H<sub>2</sub> and CO mixture) as raw material to produce synthetic green petroleum oils for use as fuels and lubricants is increasing more and more [9–12]. Simultaneously, the progress in PEMFC and SOFC systems [13,14] and in the synthetic fuel production has been improved by making hydrogen/syngas production from the fuel processing of fossil fuels, as well as biomass, more important [15–23]. Therefore, the development of efficient and compact fuel processors, capable to produce hydrogen or syngas from the reforming of different hydrocarbons, represents a significant challenge to the introduction of FCs on the market and to the growing of the hydrogen economy [1,12,24–27].

\* Corresponding author. Tel.: +39 090624297; fax: +39 090624247.

E-mail addresses: [antonio.vita@itae.cnr.it](mailto:antonio.vita@itae.cnr.it), [vitaantonio72@gmail.com](mailto:vitaantonio72@gmail.com) (A. Vita).

H<sub>2</sub> production from hydrocarbons is based on the following fundamental processes: Steam Reforming (SR), Dry Reforming (DR), Catalytic Partial Oxidation (CPOX) and autothermal reforming (ATR). SR is the most widely used process to produce syngas with a high H<sub>2</sub>/CO molar ratio (>3); low start-up and high energy consumptions are the main drawbacks. DR process becomes advantageous compared to SR when lower H<sub>2</sub>/CO molar ratios are preferable, as feed for the Fischer–Tropsch synthesis, but has the disadvantage of fast deactivation of catalysts [9,11,25,28]. CPOX process, despite high conversion and selectivity values and the very short residence time [29–31], presents several limits, as the risk of explosion and hotspot formation, with consequent catalyst deactivation and loss of activity [32]. ATR and/or Oxy–Steam Reforming (OSR) combine the effects of both the endothermic SR and the exothermic CPOX by feeding the fuel together with the oxidant (air or oxygen) and steam [33–39]. It offers several advantages over other reforming alternatives: small unit size, lower energy requirements, lower operational temperature, easier start-up, and a wider choice of materials, coupled with the possibility to regulate the H<sub>2</sub>/CO molar ratio by changing the inlet gas composition [40,41]. As the thermal energy generated by the CPOX is absorbed by the SR, the overall process results thermo-neutral (ATR). When manipulating the reaction feeding (steam-to-carbon S/C and oxygen-to-carbon O/C molar ratios) the global process can result exothermic or mildly endothermic (OSR). Besides, with the use of steam, coke formation is reduced and the hydrogen yield results increased.

Industrially, hydrogen production is generally conducted by SR of natural gas over nickel based catalysts with metal concentration as high as 10% on different oxide carriers, as Al<sub>2</sub>O<sub>3</sub> and SiO<sub>2</sub> [42–46]. However, Ni catalysts are prone to deactivation principally by carbon deposition and sintering phenomena [47,48]; while noble metal based catalysts are capable of delivering the same or better catalytic performance compared to Ni. Pt, Pd, Rh, and Ru catalysts are very active towards reforming reactions and deliver better performance than Ni at very low concentrations resulting more resistant to coke formation [49–54]. One approach to minimizing carbon formation in hydrocarbons reforming processes (SR, ATR, OSR) is by changing the process conditions, such as increasing the S/C molar ratio [55,56]. Of course, this option will result in an increase of the energy consumption and processing cost. Another approach is to use carbon resistant-catalysts. Commercial  $\gamma$ -Al<sub>2</sub>O<sub>3</sub> is widely used as carrier for noble metal and Ni catalysts due to its high specific surface area, but, to minimize carbon formation in the reforming reactions, different oxides, pure and in mixed solid solution, are being explored as potential candidates for metal carrier [57–63]. CeO<sub>2</sub> is considered a good support for the development of reforming catalysts due to its unique features associated to the oxygen mobility and storage capacity together with strong metal interaction due to the formation of metal-carrier redox couples [64–67], that can help to minimize the carbon formation [68,69].

Industrial reactors are mainly constituted by catalysts in pellet form; this configuration presents some issues related to heat and mass transfer limitations, especially at high gas flow rates [29]. To increase the overall hydrogen production, the volume and the weight of catalysts must be dramatically increased, with considerable increasing of costs. For this reason process intensification is still required to achieve good performance targets for small-scale applications such as for distributed or mobile hydrogen production [22,25,70]. Different configurations (foams, honeycombs, gauze, microchannels) were proposed as alternative to traditional packed-bed reactors [71–78]. Among these, monolith-based reactors offer many advantages, providing an efficient heat transfer within the reactor to: (i) prevent the formation of hot spots which deteriorate the overall performance, and (ii) increase the thermal efficiency of the endothermic reactions. Besides, the easy flow

of reactants inside the channels limits the pressure drops, which became one or two orders of magnitude less than those obtained with packed-beds. Furthermore, the large surface-to-volume ratio leads to good heat and mass transfer properties, allowing the use of small and compact reactors, interesting for small-scale applications [25,77–79].

One of the critical issues for the fabrication of structured catalytic beds is the deposition of suitable active layers on the carrier, capable to withstand critical reaction conditions (oxidative environment, high temperature) and, in some cases, mechanical vibrations to assure good stability. Among different deposition methods, the washcoating of slurry containing the active catalyst on ceramic monoliths is the most popular [78–80]. Many parameters and properties of the slurry must be controlled for obtaining uniform, reproducible and mechanically stable washcoating, including: pH, particle size, viscosity, slurry concentration, primers and binders utilization. Alternative methods to overcome possible drawbacks of washcoating procedure such as long preparation time, binder and primer utilization, powder manipulation, undesired catalysts modification, should be developed. In previous works [32,50,63,77,81,82], considerable performance of different catalysts in powder form prepared by solution combustion synthesis (SCS), or by SCS followed by a Wet Impregnation (WI), have been reported for different reforming processes. Characteristics of the SCS method are the fast and self-sustained strongly exothermic reactions, the use of low cost materials and the achievement of catalytic materials with metal particles well distributed on the carrier surface [81,82].

In this work, the performances of structured catalysts, based on Rh, Pt, Ni (noble metals load equal to 1.5 wt.%, Ni load equal to 7.5 wt.%) supported on CeO<sub>2</sub>, coated on cordierite monoliths (400 cpsi, diameter 1 cm, length 1.5 cm) were investigated. The monoliths were prepared by combining the SCS [81,82] with the WI technique. The physical and mechanical properties of the structured catalysts (in the fresh and used status) were investigated by X-Ray Diffraction (XRD), CO chemisorption, Nitrogen adsorption (BET), Transmission Electron Microscopy (TEM), Scanning Electron Microscopy (SEM), ultrasonic and pressure drop tests, respectively. The catalytic activity towards the methane OSR was addressed for all of the prepared catalytic monoliths: the influence of the weight space velocity (WSV) and of the reaction temperature on the catalytic performance was evaluated.

## 2. Experimental

### 2.1. Structured catalysts preparation

Conventional 400 cpsi cordierite monoliths (62 cells per cm<sup>2</sup>), with a channel diameter of 1 mm and wall thickness of 180  $\mu$ m, supplied by Applied Ceramics Inc. (USA), were used as support for the coating of catalytic layers based on CeO<sub>2</sub> carrier impregnated with active metals (Rh, Pt or Ni). All of the monoliths were first cut into cylinders of 1 cm diameter and 1.5 cm length (average weight 500 mg). As cleaning procedure, before proceeding with the deposition of the carrier layers, the cut monoliths were washed in ultrasonic bath in water/acetone (50–50 wt.%) for 30 min. Then, the monoliths were dried in a stove at 120 °C for one hour. The CeO<sub>2</sub> carrier layers were deposited by SCS [81,82] at 600 °C after dipping each monolith in a aqueous solution containing cerium nitrate (Ce(NO<sub>3</sub>)<sub>3</sub>·3H<sub>2</sub>O, Carlo Erba) as precursors and urea (CO(NH<sub>2</sub>)<sub>2</sub>, Carlo Erba) as fuel. The amount of urea and ceria precursors were calculated according to the dictates of propellant chemistry setting the so-called elemental stoichiometric coefficient  $\phi$  (the ratio between the total valences of fuel, i.e., urea, and the total valences of oxidizers, i.e., nitrates)

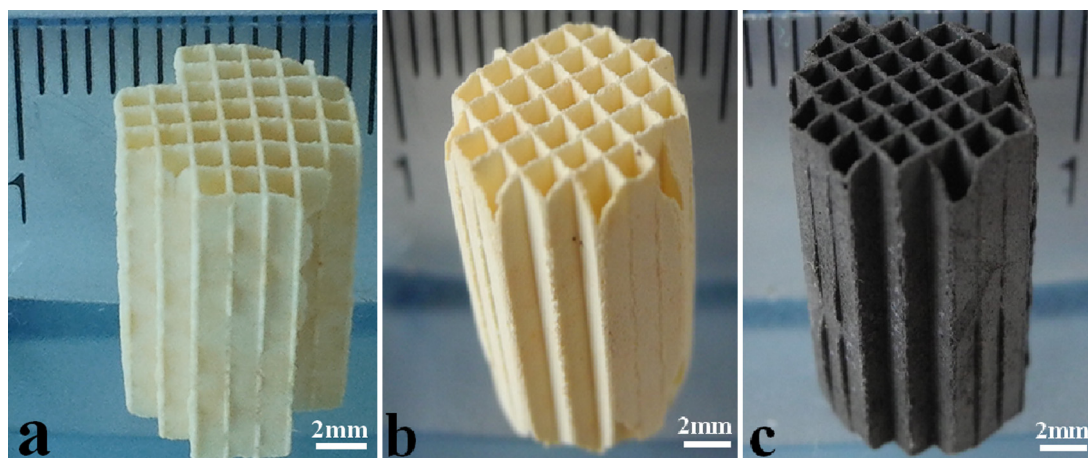


**Fig. 1.** Photographs of uncoated monolith (a), coated monolith with CeO<sub>2</sub> after combustion synthesis and calcination at 600 °C (b), final structured catalyst after the impregnation of the metal precursor (Ni(NO<sub>3</sub>)<sub>2</sub>·6H<sub>2</sub>O) and the final calcination at 400 °C (c).

equal to 1 [81–83]. For the deposition of ceria carrier 2 ml of a solution 3 M of Ce Ce(NO<sub>3</sub>)<sub>3</sub>·6H<sub>2</sub>O (from Alfa Aesar) was used. The carrier deposition process was repeated several times until the desired amount of CeO<sub>2</sub> was reached. In detail, five cycles were necessary to achieve a weight gain of about 27.6% respect to the total weight of the monolith. The obtained increase in weight was about 5.5% (respect to the final monolith weight) after each cycle (dipping/combustion). The coated samples were then calcined at 600 °C in static air for 2 h. Regarding the amount of ceria carrier loaded on monoliths, this value is connected to our previous investigation with 1.5 wt.% Ru/Al<sub>2</sub>O<sub>3</sub> monolith [84]. To determine the optimal catalyst load (including ceria carrier and active metal), three cordierite monoliths prepared with different loads of 1.5 wt.% Ru/γ-Al<sub>2</sub>O<sub>3</sub> catalyst (respectively, 5.0, 6.5, and 7.2 mg cm<sup>−2</sup> on the bare monolith) were tested towards the CH<sub>4</sub> OSR reaction. The results pointed out that a load of 6.5 mg cm<sup>−2</sup> (corresponding to a final total carrier loading equal to about 27.6%) was adequate to achieve a very good catalytic performance for the adopted conditions. The active metal phases were then added by WI technique, by dipping the coated monoliths into an aqueous solution (2 ml) containing the exact amount of the desired active metal loading (calculated respect to the ceria carrier previously loaded) in the form of solubilized precursors (RhCl<sub>3</sub>·xH<sub>2</sub>O from Sigma Aldrich, H<sub>2</sub>PtCl<sub>6</sub> by Engelhard, Ni(NO<sub>3</sub>)<sub>2</sub>·6H<sub>2</sub>O by Carlo Erba). About three cycles of immersion–blowing–drying were needed, to completely consume the solution, to obtain the desired amount of active metal: 1.5 wt.% for the noble metals, (Rh and Pt), and 7.5 wt.% for Ni, respect to the deposited weight of the carrier. The monoliths were finally calcined at 400 °C in static air for 2 h, reaching at the end of the deposition process a total catalyst load of 6.5 mg cm<sup>−2</sup> (referred as weight of active metal plus oxide carrier on the bare monolith geometric surface), with a noble metal load of about 0.1 mg cm<sup>−2</sup> and nickel load of about 0.48 mg cm<sup>−2</sup>. Fig. 1 shows the photographs of the uncoated monolith (a), the coated monolith with CeO<sub>2</sub> after the SCS and calcination at 600 °C (b), the structured Ni-based catalyst after the impregnation with the metal precursor Ni(NO<sub>3</sub>)<sub>2</sub>·6H<sub>2</sub>O and the final calcination at 400 °C (c). Together with the preparation of the coated monoliths (two types per metal loaded, one for catalytic tests and the other for morphological characterization), the corresponding catalysts were prepared at powder level, to be used for the chemical–physical characterization. The preparation sequence and the solutions concentration used for the powders synthesis were equal to those used for the deposition of the active layer on cordierite monoliths, in order to have powders with comparable chemical–physical properties.

## 2.2. Physical–chemical and mechanical characterizations

The XRD patterns were collected on the catalysts at powder level and on structured form (after crashing and grinding in an agate mortar) form using a Philips X-Pert 3710 diffractometer equipped with a Cu Kα radiation at 40 kV and 30 mA. All of the powder samples were scanned over 2θ range between 20° and 75° over 1 h. The peaks were assigned according to the PCPFWIN database. The mean crystallite size *d* was related to the pure X-ray broadening (*β*) by the Scherrer equation (1): the half maximum line width from pure CeO<sub>2</sub> (1 1 1) reflecting planes was used.

$$d = \frac{k \cdot \lambda}{\beta \cdot \cos \theta} \quad (1)$$

The half maximum line width from pure CeO<sub>2</sub> (1 1 1) reflecting planes was used.

The specific surface areas of the catalysts were determined using the Brunauer–Emmet–Teller (BET) method within the relative pressure range of 0–1 (ASAP 2020 M Micromeritics) on the catalysts in powder form. Nitrogen adsorption isotherms were recorded at −196 °C. Prior to adsorption, approximately 50.0 mg of powder was placed in the cell and evacuated at 350 °C for 3 h under high vacuum.

By using the same apparatus, the chemisorption analysis was carried out, in order to evaluate the active metals dispersion on the carriers. H<sub>2</sub> saturation was first performed by flowing 20 Ncm<sup>3</sup> min<sup>−1</sup> of H<sub>2</sub> for 2 h at 350 °C, and at the end, a He flow rate of 20 Ncm<sup>3</sup> min<sup>−1</sup> for 1.5 h was fed to the apparatus increasing the temperature up to 370 °C. Then, at room temperature, a mixture of 10% CO in He was injected in pulses of 500 NμL each, until the fulfilment of constant outlet peaks. The amount of adsorbed gas was determined as the difference between the total injected volume and the residual escaped one. The metal dispersion *D* (%) on the carrier surface was determined as follows:

$$D(\%) = S_f \frac{V_{ads} \cdot M_{me}}{V_g \cdot F_{me}} \cdot 100 \quad (2)$$

considering that the stoichiometric factor *S<sub>f</sub>* is equal to 1 (i.e., each metal atom adsorbed one CO molecule), the total volume of CO chemisorbed refers to the mass of the carrier used for the analysis in Ncm<sup>3</sup> g<sup>−1</sup> (*V<sub>ads</sub>*), the metal atomic weight *M<sub>me</sub>* of the employed active metals (Rh = 102.91 g mol<sup>−1</sup>, Pt = 195.08 g mol<sup>−1</sup>, and Ni = 58.69 g mol<sup>−1</sup>), the total mass fraction of the metal on the catalyst *F<sub>me</sub>* (expressed as g<sub>me</sub> g<sup>−1</sup> of carrier), and that one gas g-mole, *V<sub>g</sub>*, occupies 22,414 cm<sup>3</sup> at normal conditions.

The morphology of fresh and used catalytic layers scraped from monoliths were analyzed by TEM using a Philips CM12 instrument. Specimens were prepared by ultrasonic dispersion of the layers powder in isopropyl alcohol by depositing a drop of suspension on a holey copper grid. The powders for the specimens preparation were removed by a strong mechanically scraping from different internal walls of the fresh (after reduction procedure) and the used monoliths. Mean metal particle size, calculated as the surface-area weighted diameter ( $d_s$ ), was derived according to:

$$d_s = \frac{\sum_i n_i \cdot d_i^3}{n_i \cdot d_i^3} \quad (3)$$

The morphology of the coated layers on the monoliths was examined by SEM-EDX technique. A FEI XL 30 microscope equipped with a field emission gun and EDX probe was employed. Measurements were carried out at an accelerating voltage of 20 kV. The samples were positioned on the stub to obtain a frontal view of the channels and they were cut longitudinally to observe the morphology of the internal coated walls.

The pressure drop at different superficial velocities across the bare cordierite and the prepared coated monoliths was determined by a water-filled U-tube manometer connected to a quartz tube (equal to the one used for the catalytic tests) containing the monolith on one side, and open to the atmosphere on the other side.  $N_2$  flow was supplied at ambient temperature by a mass flow meter (Brooks) and measured by a digital flow-meter (ADM 2000). The difference in the heights of the two sides of the water-filled U-tube manometer was supported by the pressure drop in the monolith, and measured with a sub-millimetric scale. The experimental values were compared to the theoretical ones obtained by the application of the Hagen–Poiseuille equation to the commercial cordierite used as support in this study [85,86]:

$$\frac{\Delta p}{L} = \frac{32 \cdot \eta}{d_p^2 \cdot \varepsilon} \cdot \omega \quad (4)$$

where  $\Delta p$  is the pressure drop (Pa),  $L$  the monolith length (m),  $\eta$  the fluid dynamic viscosity (Pa s),  $\varepsilon$  the bed voidage (dimensionless),  $d_p$  the hydraulic diameter of the elementary channel (m), and  $\omega$  the superficial velocity ( $m s^{-1}$ ). The  $\varepsilon$ , equal to 0.71, was estimated through an He picnometer (Micromeritics).

On coated monoliths, the adherence between the catalytic layer and the cordierite walls was evaluated determining the monolith weight loss after ultrasonic treatment: each monolith was dipped into a solution of 50% isopropyl alcohol and 50% water, and sonicated at 45 kHz and 130 W for 30 min in a ultrasonic device (USC 900D VWR International), according to a method described in the literature [85]. After the ultrasounds treatment, the monoliths were dried at 120 °C in static air for 30 min. Then, the sonication treatment was repeated a second time. The weight loss was evaluated by measuring the weight ( $W$ ) of the monoliths before and after the ultrasonic treatment.

### 2.3. Reactivity of the structured catalysts towards OSR

The  $CH_4$  OSR experiments were carried out in a fixed-bed quartz reactor with inner diameter of 1 cm at atmospheric pressure. The structured catalysts were placed between two quartz wool plugs in the centre of the quartz tube, inserted into a furnace heated at the reaction temperature  $T_{SET}$  and controlled through a PID temperature controller. The reaction temperature was measured and controlled by three chromel–alumel thermocouples. One thermocouple was centred within the catalyst bed to regulate the  $T_{SET}$ , while the others two were kept just at the inlet and the outlet to monitor  $T_{IN}$  and  $T_{OUT}$  during the reaction. The catalytic tests, for

each prepared monolith, were divided in two series, for an overall time-on-stream (TOS) of about 60 h.

A first series of catalytic tests were carried out at different  $T_{SET}$ , ranging between 500 and 800 °C, with fixed weight space velocity ( $WSV = 65,000 Nml g_{cat}^{-1} h^{-1}$ ), fixed molecular oxygen-to-carbon molar ratio ( $O/C = 0.55$ ) and fixed steam-to-carbon molar ratio ( $S/C = 1.2$ ). A second series of the experiments were carried out by varying the WSV between 33,000 and 400,000  $Nml g_{cat}^{-1} h^{-1}$  at fixed  $T_{SET}$  (800 °C), fixed  $O/C$  (0.55), and fixed  $S/C$  (1.2). The flow rates varying between 100 and 1100  $Nml min^{-1}$  were regulated by mass flow controllers (Brooks Instrument Smart Mass Flow). High purity gases  $CH_4$ ,  $O_2$  and  $N_2$  (99.999% from SIAD, with  $N_2$  in a ratio to simulate the air composition) were used in the experiments. The steam was added to the feed by using an isocratic pump (Agilent 1100 Series) and a specially designed evaporator. The feed and reaction products were analyzed using an Agilent 6890 Plus gas chromatograph equipped with thermal conductivity (TCD) and flame ionization detectors (FID). The  $CH_4$ , revealed in both detectors, was used as internal reference for mass balance calibration, together with the  $N_2$  peak.

Before testing the catalytic performance of the prepared monoliths, each coated monolith was reduced under hydrogen-rich atmosphere directly in the quartz reactor of the test rig according to the following procedure: heating-up of the reactor at 200 °C with a  $N_2$  flow rate of 100  $Nml min^{-1}$ , staying at 200 °C for 1 h with a flow rate of 200  $Nml min^{-1}$  composed of 50%  $H_2$  and 50%  $N_2$ , further heating-up of the reactor up to the  $T_{SET}$  of 800 °C with a  $N_2$  flow rate of 100  $Nml min^{-1}$ , and then start-up of the OSR reaction tests. At the achievement of the  $T_{SET}$ , the  $N_2$  flow rate was stopped and the mixture of reagents was fed to the reactor. On-line chromatographic analysis of the reaction products was carried out every 20 min during each test. Measurements were repeated at least three times per configuration, to assess the reproducibility of the results. The carbon balance was always closed within  $\pm 2\%$ . The methane conversion ( $X_{CH_4}$ ) was calculated according to the following equations:

$$X_{CH_4} (\%) = \frac{F_{CH_4, in} - F_{CH_4, out}}{F_{CH_4, in}} \times 100 \quad (5)$$

where  $F_{CH_4, in}$  and  $F_{CH_4, out}$  are the inlet and outlet molar flow rate of methane measured at the inlet or outlet of the reactor. The typical duration of each catalytic experiment was 6 h.

At the end of the experiments the reactor was switched off and cooled down to room temperature by flowing 100  $Nml min^{-1}$  of  $N_2$ . The experimental results were reported as methane conversion ( $X_{CH_4}$ ), molar concentrations of  $CH_4$ ,  $CO$ ,  $CO_2$  and  $H_2$  (on dry basis and  $N_2$ -free),  $H_2/CO$  molar ratio,  $T_{IN}$  and  $T_{OUT}$  profiles. Thermodynamic equilibrium values, calculated by a free steady-state simulation package named Aspen Plus® by AspenTech, based on the minimization of Gibbs free-energy of each of the existing species ( $CH_4$ ,  $O_2$ ,  $H_2O$ ,  $CO_2$ ,  $CO$ ,  $H_2$ , solid carbon) at the operative conditions of the catalytic monolith, were reported as comparison, too.

## 3. Results and discussion

### 3.1. Physical–chemical characterization of the catalysts in powder form

The specific surface area  $S_{BET}$  and the metal dispersion  $D$  for all of the catalysts prepared in powder form are reported in Table 1. The relatively low  $S_{BET}$  values can be attributed to the low  $S_{BET}$  values of the  $CeO_2$  carrier [86–88], due to the high temperatures reached during the SCS [32]. Interesting to note that as the Rh- and Pt-based monoliths presented very similar  $S_{BET}$  values, the Ni-based one was three times lower: its lower specific surface area can be attributed to the higher metal loaded that probably covered

**Table 1**

Physical characterization of the prepared catalysts at powder level from XRD, BET, CO chemisorption analyses. EDX values were obtained with the structured catalysts.

Sample	Crystallite size	$S_{\text{BET}}$	$D$	EDX
	CeO <sub>2</sub> (nm)	(m <sup>2</sup> g <sup>−1</sup> )	(%)	Me/Ce atomic ratio
1.5 wt.% Rh/CeO <sub>2</sub>	17	14.3	22.2	0.025
1.5 wt.% Pt/CeO <sub>2</sub>	16	16.1	23.1	0.011
7.5 wt.% Ni/CeO <sub>2</sub>	19	5.3	2.9	0.27
CeO <sub>2</sub>	20	18	–	–

a larger number of pores. Regarding the noble metal dispersion, as the Rh/CeO<sub>2</sub> and the Pt/CeO<sub>2</sub> catalysts presented relatively high values, 22.2 and 23.1% respectively, the Ni/CeO<sub>2</sub> catalyst instead showed a lower value 2.9%. The CeO<sub>2</sub> carrier is well known to play a synergetic role in enhancing the metal dispersion [87–90], as for the case of Rh and Pt, but in the case of the Ni-based catalyst, most probably the high amount of metal loaded contributed to reduce the dispersion through the formation of bigger particles. Similar values in terms of both the  $S_{\text{BET}}$  and the  $D$  were obtained recently on similar catalysts by Amjad et al. [63].

XRD analysis was used to identify the crystal phases of the prepared catalysts in powder and structured form, the related patterns shown in Fig. 2 are compared with pure ceria (2a) synthesized by the same SCS method and monolith (cordierite) support (2b). For all of the prepared samples in powder form, Fig. 2a, the fluorite oxide type structure, with a fcc unit cell corresponding to the (1 1 1), (2 0 0), (2 2 0), (3 1 1), (2 2 2), and (4 0 0) planes (pure CeO<sub>2</sub>, JCPDS card no. 81-0792,  $2\theta = 28.54^\circ$ ,  $33.07^\circ$ ,  $47.47^\circ$ ,  $56.33^\circ$ ,

$59.07^\circ$ ,  $69.40^\circ$ ) was identified as the principal phase. For the 1.5% Rh/CeO<sub>2</sub> catalyst no peaks due to the Rh phases can be envisaged, suggesting that the Rh dispersion was high (as confirmed by the high value reported in Table 1,  $D = 22.2\%$ ). A slight shift of the ceria reflection to higher degrees ( $2\theta = 28.70^\circ$  for the (1 1 1) CeO<sub>2</sub> plane) compared to pure CeO<sub>2</sub> can be envisaged, an evidence of a change in the lattice parameters probably due to the partial incorporation of Rh (Rh<sup>4+</sup> ionic radius = 0.06 nm) into the CeO<sub>2</sub> lattice (Ce<sup>4+</sup> ionic radius = 0.097 nm), forming a partial solid solution that caused the observable peaks' shift [59,65,89]. Similar behaviour was evidenced by the diffraction patterns of the Pt-based catalyst reported in Fig. 2: as for the Rh-based catalyst, the CeO<sub>2</sub> reflections were slightly shifted to higher degrees ( $2\theta = 28.77^\circ$  for the (1 1 1) CeO<sub>2</sub> plane, Pt<sup>4+</sup> ionic radius = 0.062 nm) compared to those of pure CeO<sub>2</sub>. Additionally, Pt metal and oxides phases were absent: this may be due to the low loading or can denote a relatively good metal dispersion in the catalyst (see Table 1) [50,56,90]. Conversely, with the Ni/CeO<sub>2</sub> catalyst the diffraction patterns showed broadening peaks relative to the principal NiO diffraction line (JCPDS card no. 4-835,  $2\theta = 37.27^\circ$ ,  $43.29^\circ$ ,  $62.91^\circ$ ), the related value of the crystallite sizes, as calculated using Scherrer equation on the NiO 200 diffraction reflection, corresponded to 23 nm. As expected, the presence of NiO reflections in the diffraction pattern of Ni based catalyst can be mainly due to the higher metal loading respect to the other noble-metal catalysts (7.5 wt.% instead of 1.5 wt.%). Also for the Ni-based sample the reflection lines of the CeO<sub>2</sub> were slightly shifted to higher degrees ( $2\theta = 28.75^\circ$  for the (1 1 1) CeO<sub>2</sub> plane, Ni<sup>2+</sup> ionic radius = 0.69 Å) compared to those of pure CeO<sub>2</sub> [91,92]. Similar results on Ni/CeO<sub>2</sub> catalysts prepared by SCS were obtained by Pino et al. [66]. In Table 1 it is also reported the mean crystallite size of ceria for all of the prepared samples calculated according to the Scherrer equation (1). These values were close to that of pure CeO<sub>2</sub> carrier, prepared by the same SCS technique: no particular modification of the carrier occurred after the WI step.

### 3.2. Physical–chemical and mechanical characterization of the structured catalysts

Comparing the patterns of the catalysts in powder form (A, B, C) with those of the structured samples (A', B', C'), no relevant differences can be envisaged about the Me(Rh, Pt, Ni)/CeO<sub>2</sub> catalysts. However, as expected and evident in Fig. 2b, comparing the three patterns with that corresponding to the bare monolith support, overlapping between the signals attributed to the cordierite and those of the catalytic layers can be observed, especially about the main peak (1 1 1) of the CeO<sub>2</sub> carrier. Instead, the others diffraction peaks (2 2 0), (3 1 1), (2 2 2), and (4 0 0) are clearly visible for all the structured catalysts.

The morphology and the metal particle size of the as-prepared catalytic layers were investigated by TEM on the powder obtained by mechanically scraping different internal walls of fresh monoliths after the reduction step. The relative micrographs are shown in Fig. 3. TEM measurements showed that the Rh/CeO<sub>2</sub> (Fig. 3a) and Pt/CeO<sub>2</sub> (Fig. 3b) layers presented well dispersed and small metal particles with size ranging prevalently from 3.9 to 7.2 and 4.2 to 7.6 nm, respectively, providing a mean particle size of 5.5 nm for the Rh and 5.8 nm for the Pt. The micrograph of the Ni/CeO<sub>2</sub> layer (Fig. 3c), instead, showed a substantial number of large Ni particles with different and irregular sizes over the CeO<sub>2</sub> carrier. Particle's size ranged between 9.3 and 21.5 nm with a mean Ni particle size of 18.8 nm. The presence of larger Ni metal grains compared to those found for the Rh and Pt noble metals confirmed the influence of Ni loading on the final morphology of the catalyst itself. These data were consistent with the XRD and chemisorptions results reported in Fig. 2 and Table 1, respectively.

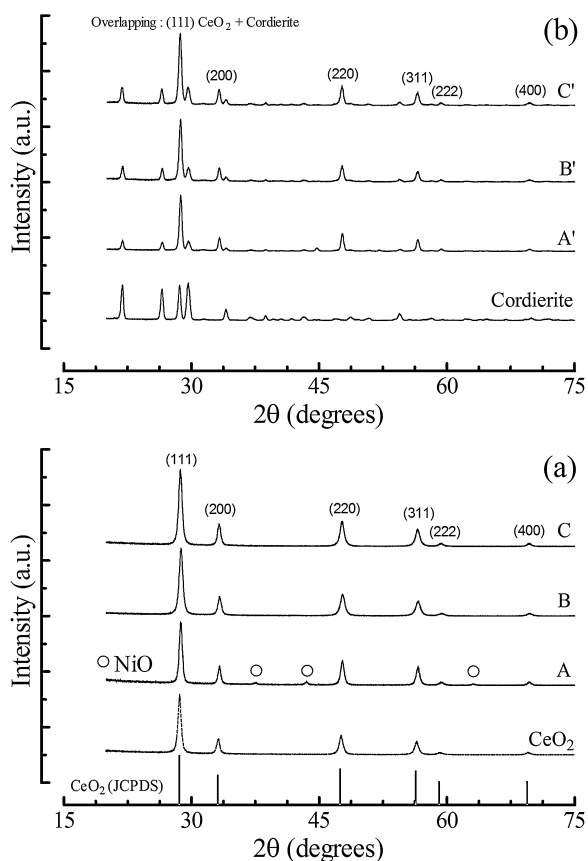


**Fig. 2.** XRD patterns of the powder catalysts (A = 7.5 wt.% Ni/CeO<sub>2</sub>, B = 1.5 wt.% Pt/CeO<sub>2</sub>, C = 1.5 wt.% Rh/CeO<sub>2</sub>) compared to the peak position of the pure CeO<sub>2</sub> carrier (reference CeO<sub>2</sub> phase: JCPDS 81-0792) (a). XRD patterns of the structured catalysts (A' = 7.5 wt.% Ni/CeO<sub>2</sub>, B' = 1.5 wt.% Pt/CeO<sub>2</sub>, C' = 1.5 wt.% Rh/CeO<sub>2</sub>) compared to the peak position of the cordierite support (b).

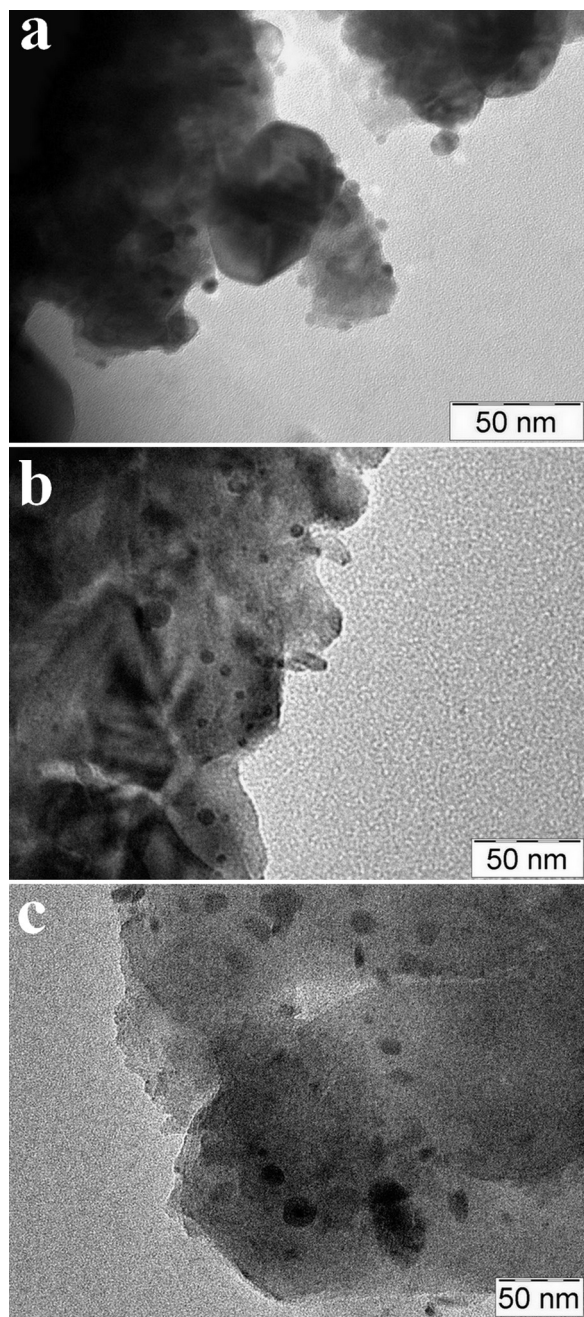


**Fig. 3.** TEM micrographs of (a) Rh/CeO<sub>2</sub>, (b) Pt/CeO<sub>2</sub>, (c) Ni/CeO<sub>2</sub> catalytic layers scraped from different internal walls of the fresh monoliths after the reduction step.

Fig. 4 shows SEM micrographs of bare cordierite monolith (A–C), monolith coated with 1.5 wt.% Rh/CeO<sub>2</sub> (D–F), 1.5 wt.% Pt/CeO<sub>2</sub> (G–I), 7.5 wt.% Ni/CeO<sub>2</sub> (J–L). Fig. 4(A–C) enlightens the plate-like morphology of the bare cordierite characterized by the presence of a macro-porosity over the surface with some connections among the pores. Such a macro-porosity remained visible even after the catalysts deposition, for all of the prepared monoliths. The micrographs of the inner channel walls (Fig. 4D, G and J) of the structured samples show in fact, that the catalytic layers were homogeneously distributed and the original monolith wall macro-porosity remains fairly unchanged, indicating that the layer thickness was very thin. The magnifications of the coating layer (Fig. 4F, I and L) confirms the presence of a significant residual macro-porosity, which could be linked to abundant and characteristic gas production that occurs during the several SCS steps [81,82]. It is also evident from the

**Table 2**

Weight loss after exposure of the monoliths to a double ultrasounds treatment (45 kHz, 130 W, 30 min for each sonication).

Sample	1 <sup>st</sup> Weight loss (%)	2 <sup>nd</sup> Weight loss (%)
1.5 wt.% Rh/CeO <sub>2</sub>	0.2	0.2
1.5 wt.% Pt/CeO <sub>2</sub>	0.2	0.3
7.5 wt.% Ni/CeO <sub>2</sub>	0.1	0.1

images that CeO<sub>2</sub> coatings, independent of the metal loaded, were strongly attached to the cordierite surface forming a thin layer that uniform cover the support. Specifically, the thickness of all of the Me/CeO<sub>2</sub> coating was estimated to be around 20–25 μm in all cases. To better enlighten the catalyst adhesion to the cordierite walls, Fig. 5 shows a magnification of the internal channel surface of the Rh/CeO<sub>2</sub> monolith. It is evident that the catalytic layer consisted of small particle clusters ranging between 0.15 and 0.30 μm, strongly connected to each other to form clusters of larger size, with a uniform distribution along the channels walls. The formation of small particle agglomerates much closer one to the others provides a more densely packed coating layer with better coating quality [78,83,86]. In addition, the results of a semi-quantitative EDX analysis of the coated layers in the different monoliths are listed in Table 1. The corresponding Me/Ce atomic ratio in the catalytic layers is close to the theoretical values; 0.026, 0.013, 0.25, calculated, respectively, for the 1.5 wt.% Rh/CeO<sub>2</sub>, 1.5 wt.% Pt/CeO<sub>2</sub>, 7.5 wt.% Ni/CeO<sub>2</sub> samples.

The mechanical stability of the catalytic active phases lined on monoliths is a critical issue for practical application purposes, especially for mobile applications, since coating loss must be avoided. Thus, the adherence and the mechanical properties of the lined catalytic coatings were evaluated by sonication, according to a method described in the literature [82]. The obtained results are reported in Table 2. All of the monoliths showed a negligible weight loss of the catalytic layers after two sonication baths. The adhesion of the layer to the cordierite surface was very strong and the coated phase resulted well anchored on the cordierite with strong resistance to vibrations and mechanical shocks. This outcome confirmed the results obtained with the SEM analysis that showed a uniform and compact layer of catalysts on the cordierite surface. The small weight loss of the monoliths can be associated to the detachment of the superficial debris of the catalytic layer. The coating adherence can be considered appropriate for all of the catalytic monoliths. Such specific mechanical property of the catalytic coating can be due to the small agglomerates, visible in Fig. 5, produced during the SCS deposition process, which resulted well anchored to the superficial porosity of the bare cordierite monolith walls, forming a uniform and compact thin catalytic layer. Thus, SCS can be considered a very suitable method to deposit catalysts onto structured catalysts, as already demonstrated even on other kind of metallic or ceramic structured supports [81,82,93,94].

Pressure drop constraints represent a relevant issue for the design of reactors capable to sustain catalytic reforming processes [22,24,95]. Typically in such applications, very high conversions must be achieved under diffusion-controlled conditions, to secure the required efficiency while keeping the pressure drop as low as possible, to avoid excessive energy losses [95,96]. To evaluate the resistance of the coating layers towards increasing flows, the pressure drop at different superficial velocities was measured for the prepared monoliths and the bare cordierite. The obtained results are reported in Fig. 6, together with the theoretical values obtained from the Hagen–Poiseuille equation (4). The superficial gas velocity was increased up to 15 m s<sup>−1</sup>, the measured pressure drops increase from 320 to 11,000 Pa m<sup>−1</sup>. All of the coated monoliths exhibited comparable pressure drops to the one of the bare cordierite monolith. In addition, the experimental results fitted quite well with the

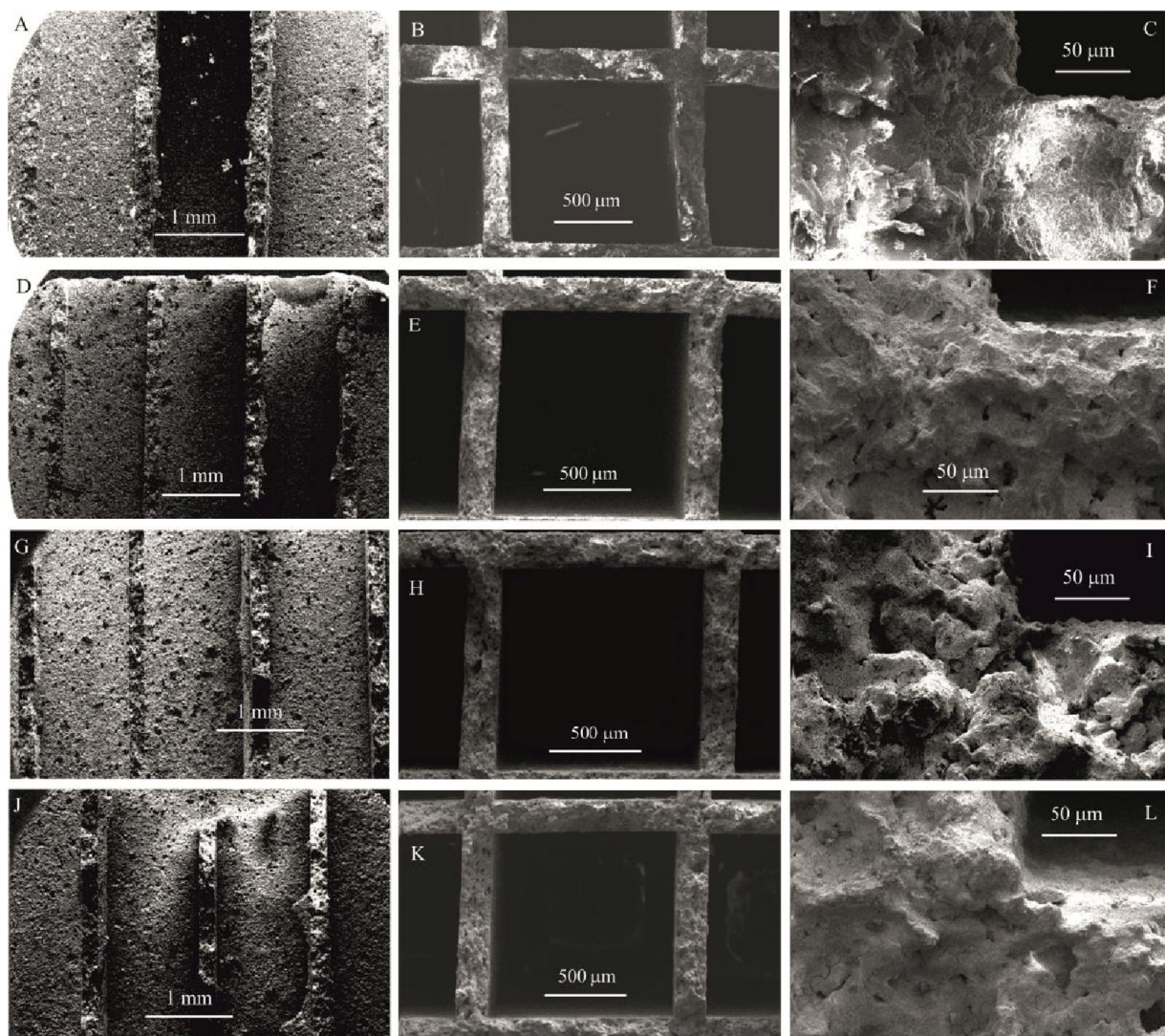


**Fig. 4.** SEM micrographs of the coated monoliths: inner channels view (A, D, G, and J), frontal channel view (B, E, H, and K), and corner channel view (C, F, I, and L). Bare cordierite (A, B, and C), Rh/CeO<sub>2</sub> (D, E, and F), Pt/CeO<sub>2</sub> (G, H, and I), and Ni/CeO<sub>2</sub> (J, K, and L).

Hagen–Poiseuille theoretical calculation: the obtained results, in fact, clearly shows that the influence of the catalytic layers on the pressure drop is minimal at low superficial gas velocities, whereas for values higher than 5 m s<sup>−1</sup> the pressure drops slightly overcome the one of the bare monolith. Thus, the influence of the catalytic layer on the pressure drop was evident at high superficial gas velocities: this effect is mostly due to an increased roughness of the cordierite surface after the deposition of catalytic layer, as visible by SEM analyses (see Figs. 4 and 5). Anyway, the measured pressure drops were relatively low, assuring a short diffusion distance inside the thin catalytic layer, resulting in greater catalyst utilization and, possibly, improved catalytic activity.

### 3.3. Reactivity of the structured catalysts towards OSR

The overall stoichiometry for the CH<sub>4</sub> OSR process involves a combination of endothermic (see reaction (6)) and exothermic reactions (see reactions (7) and (8)), followed by the establishment of the water gas shift equilibrium (see (9)): the energy generated by the oxidation reactions, in fact, is used for the endothermic SR reactions, leading to a local decrease of the temperature, which promotes the WGS equilibrium.

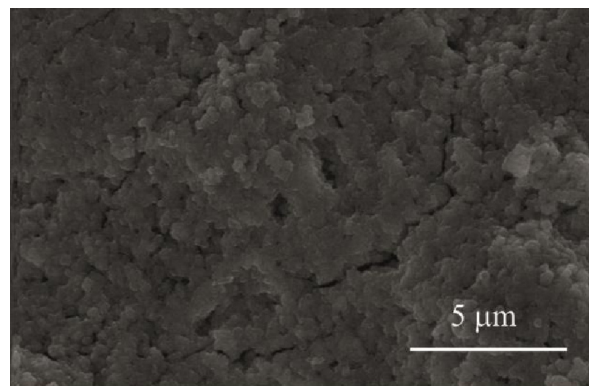


**Fig. 5.** SEM micrograph with the magnification of the inner channel surface coated with Rh/CeO<sub>2</sub>.

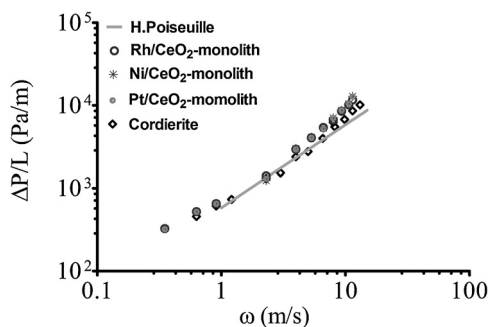
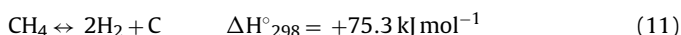
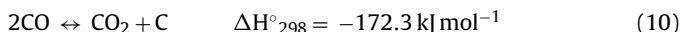


**Fig. 6.** Pressure drop measurements as a function of the superficial gas velocity on the structured catalysts and bare cordierite monolith, compared to the Hagen–Poiseuille theoretical values (continuous line).

By changing the operating parameters (temperature, O/C and S/C molar ratios) the process can be made endothermic, almost thermoneutral or mildly exothermic. Moreover, it can be conducted minimizing the carbon deposition according to the Boudouard reaction (10) or to the methane cracking reaction (11):



The addition of slight amounts of O<sub>2</sub> in OSR promotes the complete conversion of CH<sub>4</sub> and provides a faster dynamic response to requests of power changes [25,33,34,38]. Thus, according to our recent investigations [84], by maintaining fixed the molecular oxygen-to-carbon (O/C=0.55) and steam-to-carbon (S/C=1.2) molar ratios, the influence of the reaction temperature and of the WSV was investigated.

### 3.3.1. Influence of the reaction temperature

Fig. 7 shows the influence of the operative temperature ( $T_{\text{SET}}$  varied between 500 and 800 °C) on the various catalytic monoliths performances towards the methane OSR at WSV=65,000 hNm<sup>3</sup>g<sub>cat</sub><sup>−1</sup>h<sup>−1</sup>, with the molar ratios fixed at O/C=0.55 and S/C=1.2. In addition to the experimental values, the equilibrium curves are also reported in Fig. 7. The performances of all of the structured catalysts followed similar trends, approaching

the equilibrium condition values strongly depends on the reaction temperature. Analyzing more in detail the results, the effect of temperature is prevalent between 700 and 800 °C, instead, at low temperatures (500–600 °C) the relative activity of the prepared samples can be better highlighted. Increasing the temperature from 700 to 800 °C the methane conversion increased from 96.2 to 99.3% for the Ni/CeO<sub>2</sub> monolith, from 96.4 to 99.2 for the Pt/CeO<sub>2</sub> monolith, and from 96.9 to 99.4% for the Rh/CeO<sub>2</sub> monolith. A similar trend occurred for the hydrogen concentration (ranging from 67.5 to 67.9% for the Ni/CeO<sub>2</sub> monolith, from 67.8 to 68.0 for the Pt/CeO<sub>2</sub> monolith, and from 68.3 to 68.4% for the Rh/CeO<sub>2</sub> monolith). The gap of the catalytic activity, between the catalysts, became slightly larger decreasing the  $T_{\text{SET}}$ . At 600 °C the Pt-based monolith showed the lowest methane conversion and hydrogen concentration, 74.8 and 60.8%, respectively, instead the Rh-based sample the highest 80.3 and 63.6%. The performances of the Ni/CeO<sub>2</sub> monolith, at 600 °C, are intermediate between that of the other two samples with a methane conversion equal to 77.0% and a hydrogen content of 61.8%. At 500 °C the Rh/CeO<sub>2</sub> monolith approached better the thermodynamic equilibrium with the highest methane conversion and hydrogen concentration, 60.0 and 54.5%, respectively, instead the nickel based sample has showed a methane conversion of 56.7% associated with a hydrogen amount of 50.6%. Finally, the Pt/CeO<sub>2</sub> monolith has showed again the lowest performance with a methane conversion of 53.5% and a hydrogen concentration of 48.4%.

At lower temperatures, only part of the methane was converted by the complete oxidation reaction (reaction (8)), forming CO<sub>2</sub> and H<sub>2</sub>O. In this condition the hydrogen amount mainly came out from the exothermic methane partial oxidation (reaction (7)) and the water gas shift equilibrium (reaction (9)), but both the methane conversion and the hydrogen concentration remained low for all of the structured catalysts. The temperatures measured at the inlet of the catalytic monolith during the reaction, reported in Fig. 7, helped to sustain such a consideration: they were always higher (from 25 to 50 °C) compared to the  $T_{\text{SET}}$  one. The high temperature at the beginning of the catalytic monolith was of course due to the prevailing of the oxidation reactions (reactions (7) and (8)). The measured outlet temperatures of the structured catalysts were always lower than the inlet ones due the occurrence of the endothermic reactions [77,91].

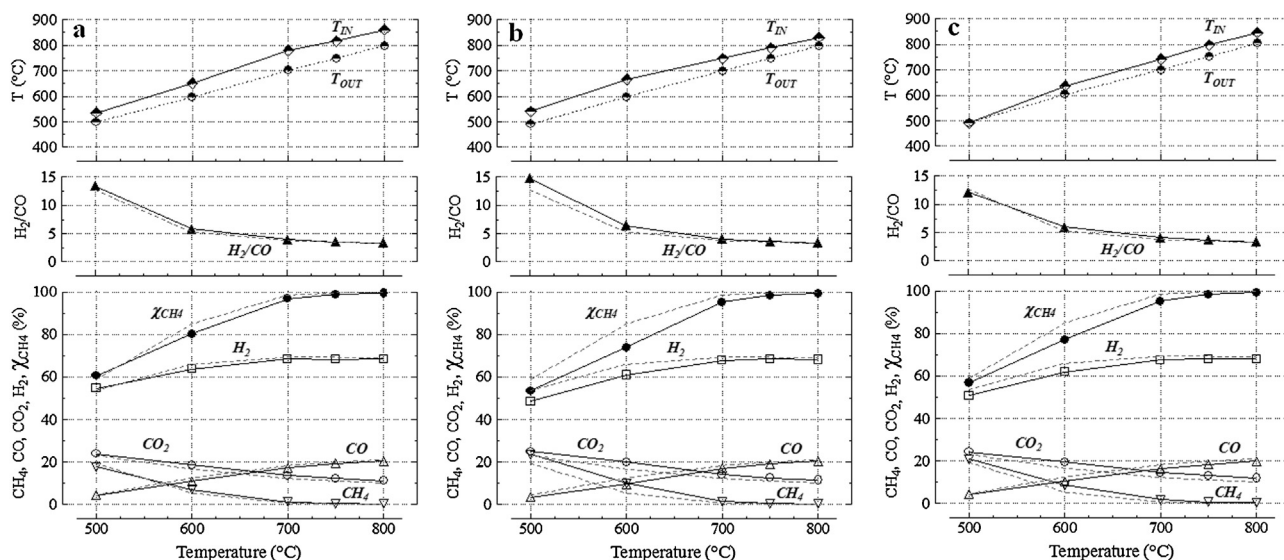


**Fig. 7.** Influence of the reaction temperature on methane conversion, syngas composition (dry and nitrogen free basis) and its H<sub>2</sub>/CO ratio,  $T_{\text{IN}}$  and  $T_{\text{OUT}}$  for the various structured catalysts: (a) Rh/CeO<sub>2</sub>, (b) Pt/CeO<sub>2</sub>, (c) Ni/CeO<sub>2</sub>. For comparison, equilibrium values are reported as dotted lines. Reaction conditions: WSV = 65,000 Nm<sup>3</sup>g<sub>cat</sub><sup>−1</sup>h<sup>−1</sup>, O/C = 0.55, and S/C = 1.2.

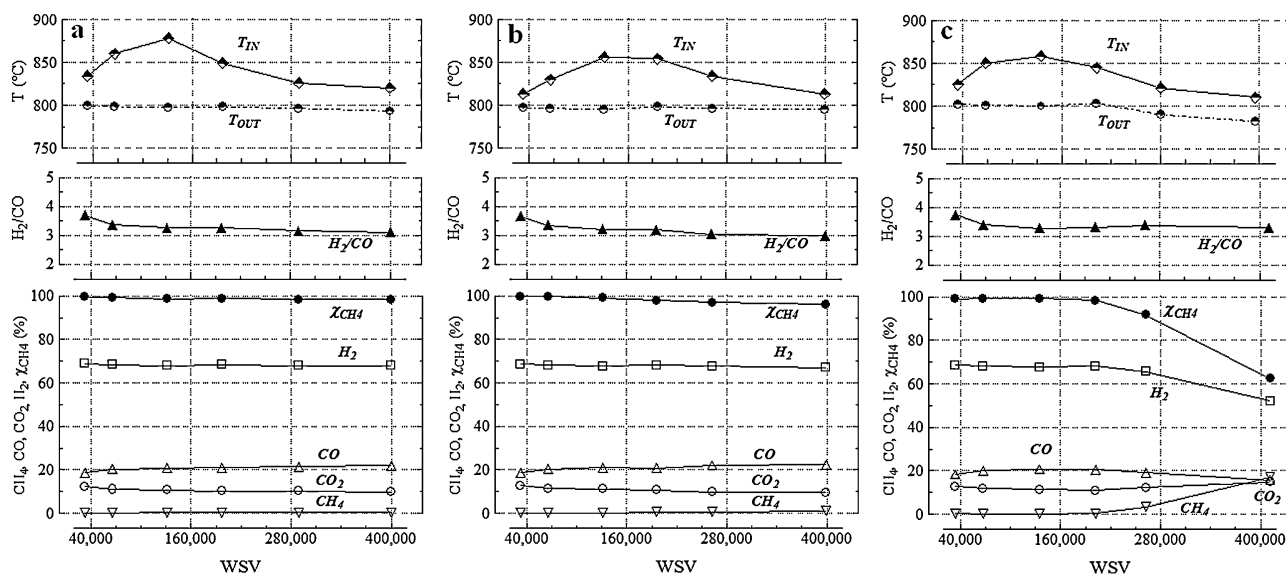


**Fig. 8.** Influence of the WSV on methane conversion, syngas composition (dry and nitrogen free basis) and its  $H_2/CO$  ratio,  $T_{IN}$  and  $T_{OUT}$  for the various structured catalysts (a) Rh/CeO<sub>2</sub>, (b), Pt/CeO<sub>2</sub>, (c) Ni/CeO<sub>2</sub>. Reaction conditions:  $T_{SET} = 800^\circ C$ ,  $O/C = 0.55$ , and  $S/C = 1.2$ .

By increasing the  $T_{SET}$  until  $800^\circ C$ , the SR and WGS reactions proceeded with different degree determining an opposite behaviour for the CO and CO<sub>2</sub> concentrations, as evident from Fig. 7, for all of the structured catalysts. The CO<sub>2</sub> amount in the products decreased as a result of the decrease of the contribution of the WGS equilibrium, favoured at lower temperatures, whereas the CO and H<sub>2</sub> concentration increased, even if with different trends, due to the SR reactions. This behaviour influenced of course the  $H_2/CO$  ratio, reported in Fig. 7, which decreased with the rise of the temperature.

Thus, even if the methane conversion and hydrogen concentration values were very similar between them, especially at high temperature, the gap became slightly larger decreasing the  $T_{SET}$  and the overall sequence of the catalytic activity was  $Rh > Ni > Pt$ . Similar trends of the catalytic activity sequence  $Rh > Ni > Pt$  were reported even by other authors for SR [97] and ATR [98] reactions: in the current tests the small excess of oxygen respect to the ATR conditions at fixed S/C did not significantly change the activity of the metals [98].

### 3.3.2. Influence of the weight space velocity

The effect of the WSV on the structured catalysts' performance was investigated at constant reaction temperature ( $T_{SET} = 800^\circ C$ ), and reactants molar ratios ( $O/C = 0.55$ ,  $S/C = 1.2$ ). The WSV was varied between 33,000 and 400,000  $Nml\ g_{cat}^{-1}\ h^{-1}$ . The Mears criterion was applied to check for the absence of external mass transfer limitations [99–101]:

$$\frac{r_{eff} \cdot d_h}{2k_g \cdot c} < 0.15 \quad (12)$$

where  $d_h$  is the hydraulic diameter of the microchannel,  $r_{eff}$  is the effective determined rate of reaction,  $k_g$  is the mass transfer coefficient and  $c$  is the concentration of the species under investigation. Considering that in the fully developed laminar flow of a microchannel, as in our case, the Sherwood-number approaches a constant value of 3.66, it is possible to determine the mass transfer coefficient, which increases as the hydraulic diameter of the microchannel decreases, with consequent lower mass transport limitations [100,101]. Thus, with a value well below 0.15, no external mass transfer can be envisaged in our case.

The results are shown in Fig. 8, where the CH<sub>4</sub> conversion, the  $H_2/CO$  molar ratio and products distribution (on dry basis

and nitrogen free) are reported. At low WSV (from 33,000 to 134,000  $Nml\ g_{cat}^{-1}\ h^{-1}$ ) all of the prepared catalytic monoliths showed similar performances. At 33,000  $Nml\ g_{cat}^{-1}\ h^{-1}$ , for example, the Rh- and the Pt-based monoliths showed the highest methane conversion, close to 100%, and the Ni-based one the lowest (99.0%). Also the product outlet concentrations were very similar, as shown in Fig. 8. By increasing the WSV the catalytic activity of the prepared monoliths slightly decreased, following a similar trend for the two noble metal based monoliths, whereas the performance of the Ni-based one worsened at the highest WSV values. Between the two noble metal based monoliths, the Rh-one performed slightly better than the Pt-based one, showing at 400,000  $Nml\ g_{cat}^{-1}\ h^{-1}$  the highest methane conversion (98.3%) and the highest hydrogen concentration (67.9%). The Ni-based monolith showed a noticeable decay of the performance, with the lowest methane conversion (62.4%) and the lowest hydrogen concentration (52.2%) coupled with traces of C<sub>2</sub>H<sub>6</sub>. Changes in the WSV led also to changes in the concentrations of the reaction products. On average, in fact, an increase of the flow rate corresponded to a slight increase of the CO outlet concentration, whereas the H<sub>2</sub> and CO<sub>2</sub> concentrations decreased. Consequently, the  $H_2/CO$  molar ratio decreased. However, as shown in Fig. 8, the observed values for the two noble metal based monoliths at different flow rates were reasonably constant, with similar trends. Instead, the performance of the Ni-based monolith remained stable up to 210,000  $Nml\ g_{cat}^{-1}\ h^{-1}$ , then at higher WSV worsened at unacceptable levels. The worsening performance of the Ni-based monolith with the high WSV can be explained considering that several phenomena could contribute to its deactivation. Of course, the low metal dispersion of Ni and its relatively large particle size (see Table 1 and Fig. 3c) could promote, after a relatively long time of operation, sintering and carbon deposition phenomena. Moreover, an oxidation of metallic nickel, with a consequent activity loss, due to the total increase of O<sub>2</sub> amount increasing the WSV, cannot be excluded.

Moreover, for both the noble metals based structured catalysts and the Ni-based one, the obtained results can be associated to the typical behaviour of the monolith reactors (low pressure drop, high surface area/volume ratio and good heat and mass transfer properties) and to the chemical–physical properties of the different catalytic layers [22,95].

The temperature profiles, reported in Fig. 8, obtained measuring the temperature at the inlet and the outlet of the monoliths during the reaction, revealed that the temperatures increased by increasing the WSV up to  $134,000 \text{ Nm}^3 \text{ g}_{\text{cat}}^{-1} \text{ h}^{-1}$ , then both the  $T_{\text{IN}}$  and the  $T_{\text{OUT}}$  decreased for all of the structured catalysts till to  $400,000 \text{ Nm}^3 \text{ g}_{\text{cat}}^{-1} \text{ h}^{-1}$ , following a similar trend. The conversion of the oxygen was always complete for all of the tested WSV. It is worth noting that the measured  $T_{\text{IN}}$  was always higher than the  $T_{\text{SET}}$  ( $800^\circ\text{C}$ ), whereas the  $T_{\text{OUT}}$  remained stable at around  $800^\circ\text{C}$  up to WSV values of  $134,000 \text{ Nm}^3 \text{ g}_{\text{cat}}^{-1} \text{ h}^{-1}$ , probably influenced by the furnace temperature, then they slightly decreased up to  $785^\circ\text{C}$ . The increase of the  $T_{\text{IN}}$  in the first part of the catalytic bed, notwithstanding the reduction of the contact time, was due to the more heat produced by the exothermic reactions occurring in the monolith upstream section: the developed heat helped to sustain the endothermic SR reactions occurring in the monolith downstream section, maintaining high methane conversion and hydrogen concentration values. Therefore, the improvement in the reactor performance can only be explained considering that the system operates in a transport-controlled regime [29,102]: the increase in mass flow rate improved mass and heat transfer within the monolith counterbalancing the entailed residence time reduction, especially in the OSR process, which principally combines CPOX with SR reactions. Therefore, the use of monolithic reactors overcomes the limitation of heat transfer (typically of packed bed reactors) since the heat of the CPOX is directly utilized by the SR reaction [73,102]. The slightly decrease of the  $T_{\text{IN}}$  at high flow rates, more evident for the Ni/CeO<sub>2</sub> monolith, was due to a reduction of the catalysts activity when the contact time became very low respect to the amount of loaded catalytic layers. Besides, it is probable that increasing the WSV the temperature of the combustion peaks resulted higher than the setting temperature ( $T_{\text{SET}}$ ) at the centre of the bed, whereby no heat was provided by the furnace to sustain the reforming reaction in the last part of catalytic bed [103]. Therefore, a decrease in  $T_{\text{OUT}}$  was recorded, despite the decrease in the methane conversion.

In those operative conditions the contribute of the CPOX reaction to the reactor temperature behaviour was not anymore able to compensate the necessary heat for the SR reactions, resulting in a slight decrease in the catalytic performances as shown by the decrease in the methane conversion and in the H<sub>2</sub> concentration reported in Fig. 8. These stressing operating conditions amplified the differences in the activity between the noble metals and the nickel catalyst, showing the limits of the prepared nickel sample.

These consideration were supported also by observing the CO and CO<sub>2</sub> outlet concentration trends: the increase of the WSV caused an increase of the CO outlet concentration accompanied by a correspondent decrease of the CO<sub>2</sub> outlet concentration, and a slight reduction of the H<sub>2</sub>/CO molar ratio (see Fig. 8), only for the two noble metal structured catalysts. The high temperature level of the monolith at all of the tested WSV, in fact, limited the WGS equilibrium (reaction (9)) by favouring the reverse-WGS reaction, contributing thus to reduce the H<sub>2</sub> content and to increase the CO amount. On the contrary, for the Ni-based monolith the increase of the WSV caused a decrease of the CO outlet concentration accompanied by a correspondent increase of the CO<sub>2</sub> outlet concentration. Besides, in presence of O<sub>2</sub> the Ni present on the surface of the catalytic layer can be oxidized [92], leading to high combustion activity and absence of reforming activity. This effect could explain the increase in the CO<sub>2</sub> concentration associated with a very low steam conversion (not showed). Conversely, Rh and Pt metal are more stable than Ni metal under oxygen atmosphere and can maintain high activity also at high WSV.

The differences between the two noble metal based monoliths performance were minimal, making difficult a correct choice between the Rh/CeO<sub>2</sub> and the Pt/CeO<sub>2</sub> catalysts. Anyway, the

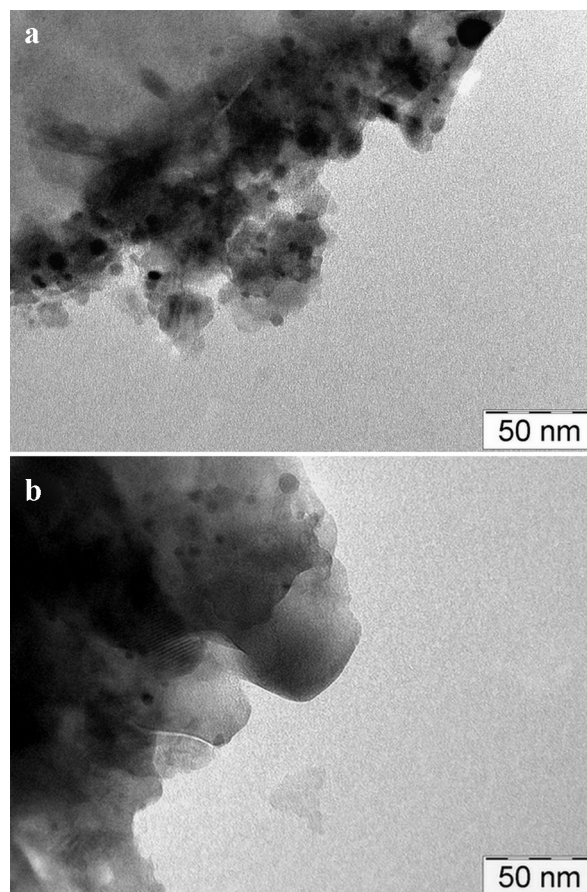
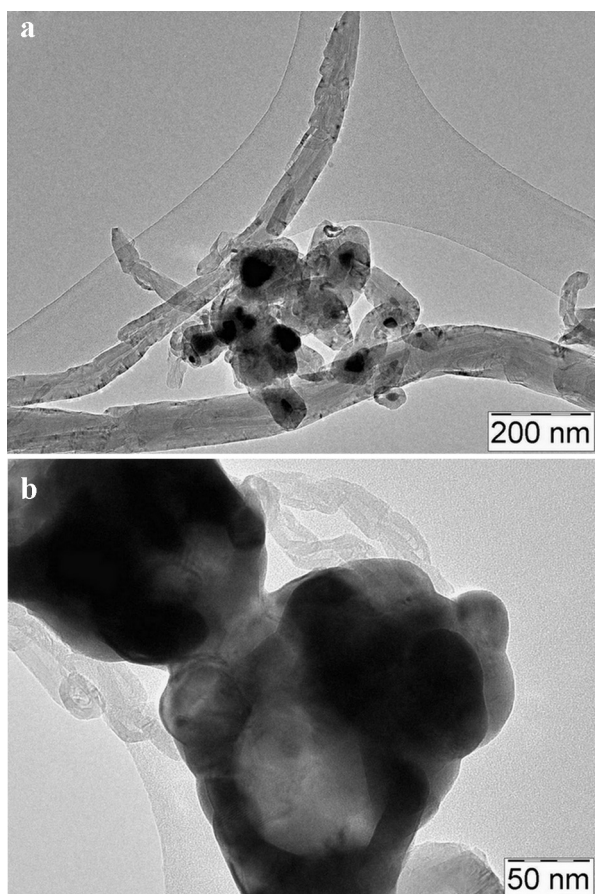


Fig. 9. TEM micrographs of (a) Rh/CeO<sub>2</sub>, (b) Pt/CeO<sub>2</sub> layers scraped from different internal walls of used monoliths after 60 h of TOS.

performance activity sequence could be  $\text{Rh} \geq \text{Pt} > \text{Ni}$ , considering the better performance of the Rh-based monolith at the highest WVS. The reported results were in line with the characterization results of fresh catalysts: the noble metal based catalysts, in fact, presented a well dispersed and small metal particles respect to the nickel based sample. This, along with the typical behaviour of noble metals (high catalytic activity and tolerance to carbon deposition), probably contributed to limit or avoid deactivation phenomena as metal sintering and carbon formation. The lowest performance activity values of the Ni-based monolith could be due to the fact that Ni-based catalysts, in the presence of oxygen, can be easily oxidized and can thereby lose their reforming activity, especially in the inlet of catalytic bed [30,91,92]. Moreover, others deactivation phenomena including coking and sintering, strictly connected with the presence of small and less dispersed metal particles, cannot be excluded, considering, also that, generally, nickel based catalysts are reported as less stable than noble metals catalysts in reforming reactions [51,54] and are more prone to coke deposition.

### 3.3.3. Used catalytic layers characterization

The effect of temperature and WSV on the catalytic layers was evaluated using the same catalytic monoliths for an overall time-on-stream (TOS) equivalent to about 60 h for each structured catalysts. Even if this TOS cannot be considered a long one, the catalytic layers were exposed to daily start-up/shut-down cycles of 6 h each, that could contribute to accelerate any possible deactivation phenomena. To investigate the morphology of the catalytic layers after the 60 h TOS, at the end of the experimental campaign the monoliths were sectioned. Some representative portions of the catalytic layers were scratched from the internal walls and analyzed



**Fig. 10.** TEM micrographs of Ni/CeO<sub>2</sub> layer scraped from different internal walls of the used monolith after 60 h of TOS: (a) encapsulated Ni particles and filamentous carbon whiskers, (b) Ni/CeO<sub>2</sub> catalyst and carbon whiskers.

via TEM. The relative images are reported in Figs. 9 and 10. By comparing the TEM micrographs of the fresh (Fig. 3a and b) and used (Fig. 9a and b) noble metals monoliths, the morphological structure of the catalytic layers did not show any relevant changes, both Rh and Pt particles appeared small and well distributed, with size ranging mainly from 4.4 to 8.7 for Rh (mean particle size of 6.4 nm), and 4.7 to 7.7 nm for Pt (mean particle size of 5.9 nm), respectively. Moreover, no carbon deposition appeared. The absence of severe particles aggregation on spent monoliths denoted that metal sintering on the carrier surface was not a dominant phenomenon for both Rh and Pt based catalysts under the investigated conditions, in agreement with the good catalytic performances recorded during the 60 h of TOS, even at high WSV (as reported in Fig. 8a and b). On the contrary, TEM micrographs of the Ni used monolith, reported in Fig. 10, provided evidence of carbon formation, both as filament whiskers [45] and in encapsulated form [104]. A good estimation of the Ni size distribution from TEM images was difficult (Fig. 10), probably due to the oxidation of nickel in presence of oxygen during the catalytic tests [91,92]. However, an indirect evaluation of the Ni particles size can be carried out considering that the size of fractured Ni particles encapsulated by carbon (Fig. 10a) ranged between 14.2 and 51.7 nm, with a mean particle size of 28.8 nm. This result pointed out huge sintering of Ni particles in the spent monolith after the catalytic activity. It is widely reported in the literature that the morphology and size of filamentous carbon, formed during the reaction, is affected by metal particle size: Kim et al. [104] have reported that 7 nm represents the minimum metal Ni particle diameter required to form filamentous carbon. Other authors have found that sintering occurred continuously during the

reforming reaction and that various forms of coke accumulated outside the sintered particles [105]. The present study confirmed that for Ni-based catalysts the formation of large Ni metal particles in the fresh catalyst and the additional sintering during the reaction may be two important factors inducing carbon whiskers formation and catalyst deactivation.

The catalytic activity coupled with the TEM analysis for all of the monoliths allowed to conclude that the best performance showed by the noble metal catalysts (particularly by the Rh/CeO<sub>2</sub> monolith) during the 60 h of reaction was associated with the maintenance of the morphological structure of the catalyst itself. On the contrary, for the Ni-based monolith the progressive carbon deposition during TOS (in particular the presence of encapsulating carbon and carbon whiskers) coupled with the metal sintering led to fast catalyst deactivation.

#### 4. Conclusions

Structured catalysts based on Me/CeO<sub>2</sub> (with Me = Rh, Pt, Ni) on cordierite honeycombs were prepared, characterized and tested towards the methane OSR reaction. The structured catalysts were prepared according to a mixed deposition process where the CeO<sub>2</sub> was lined cordierite by solution combustion synthesis (SCS) at 600 °C (27.6 wt.% by the total weight of the monolith), and the metals were lined by successive wet impregnation (WI) of the active metal phase (1.5 wt.% for the noble metal Rh and Pt, 7.5 wt.% for Ni, respect to the deposited weight of the carrier), for an overall catalyst load (metal active phase plus oxide carrier) of 6.5 mg cm<sup>-2</sup> (with a noble metal load of about 0.1 mg cm<sup>-2</sup> and nickel load of about 0.48 mg cm<sup>-2</sup>). The adopted preparation method can be considered less time consuming compared to classical deposition methods, as the washcoating technique.

The performance of the prepared structured catalysts towards the CH<sub>4</sub> OSR reaction was appreciable: the Rh- and Pt-based monoliths showed high catalytic activity and stability also at high weight space velocity (WSV). In particular, the Rh-based one performed slightly better than the Pt-one sample, maintaining high CH<sub>4</sub> conversion (98.3%) and high H<sub>2</sub> concentration (67.9%), with a H<sub>2</sub>/CO molar ratio equal to 3.2, also at the highest WSV (400,000 Nml g<sub>cat</sub><sup>-1</sup> h<sup>-1</sup>). Instead the Ni-based structured catalyst worsened its catalytic activity for WSV values higher than 210,000 Nml g<sub>cat</sub><sup>-1</sup> h<sup>-1</sup>. The worsening of the catalytic activity of the Ni-based catalysts was associated to the formation of encapsulated carbon and carbon whiskers due to fast sintering.

On the physical-mechanical point of view, the prepared structured catalysts presented a very good catalytic layer, consisting in a uniform and thin coating with thickness between 20 and 25 μm and high mechanical strength (low weight loss under ultrasonic treatment between 0.2 and 0.4 wt.%). In the present study, the use of monoliths helped to improve the catalytic performance towards the methane OSR process, especially at high flow rates: the large open frontal area, the high surface area/volume ratio, the good heat and mass transfer properties and the low pressure drop characterizing monoliths contributed to overcome the main problems of packed bed reactors (mainly heat transfer limitations). Anyway, the final performance of the structured reactor was influenced by the chemical-physical properties of the deposited catalytic layers: the best performance activity sequence can be considered as Rh ≥ Pt > Ni.

The obtained results represent a promising advance in the process intensification of fuel reforming technology: high performance at high WSV, together with relatively low cost catalysts, means designing more compact, lightweight and less expensive fuel processors.

## Acknowledgements

This work was funded by the Ministry of Education, University and Research, Italy (MIUR, Progetti di Ricerca Scientifica di Rilevante Interesse Nazionale 2010–2011) within the project IFOAMS (“Intensification of catalytic processes for clean energy, low-emission transport and sustainable chemistry using open-cell FOAMS as novel advanced structured materials”, protocol no. 2010XFT2BB).

## References

- [1] F. Barbir, *Energy* 34 (2009) 308–312.
- [2] S. Specchia, C. Francia, P. Spinelli, in: J. Zhang, L. Zhang, H. Liu, A. Sun, R.-S. Liu (Eds.), *Electrochemical Technologies for Energy Storage and Conversion*, Wiley-VCH, Weinheim, 2012, pp. 601–669.
- [3] M. Lo Faro, V. Antonucci, P.L. Antonucci, A.S. Arico, *Fuel* 102 (2012) 554–559.
- [4] W.C. Lattin, V.P. Utgikar, *Int. J. Hydrog. Energy* 32 (2007) 3230–3237.
- [5] P. Agnolucci, O. Akgul, W. McDowall, L. Papageorgiou, *Int. J. Hydrog. Energy* 38 (2013) 11189–11201.
- [6] R. Kleijn, E. Van der Voet, *Renew. Sust. Energy Rev.* 14 (2010) 2784–2795.
- [7] S. Apak, E. Atay, G. Tuncer, *Int. J. Hydrog. Energy* 36 (2012) 5481–5497.
- [8] Ö.F. Noyan, *Int. J. Hydrog. Energy* 36 (2011) 11216–11228.
- [9] Y.H. Kim, K.-W. Jun, H. Joo, C. Han, I.K. Song, *Chem. Eng. J.* 155 (2009) 427–432.
- [10] P. Nagendramma, S. Kaul, *Renew. Sust. Energy Rev.* 16 (2012) 764–774.
- [11] R.C. Baliban, J.A. Elia, V. Weekman, C.A. Floudas, *Comp. Chem. Eng.* 47 (2012) 29–56.
- [12] D.J. Roddy, *Appl. Therm. Eng.* 53 (2013) 299–304.
- [13] J. Wu, X.Z. Yuan, J.J. Martin, H. Wang, J. Zhang, J. Shen, S. Wu, W. Merida, *J. Power Sources* 184 (2008) 104–119.
- [14] M. Gandiglio, A. Lanzini, P. Leone, M. Santarelli, R. Borchellini, *Energy* 55 (2013) 142–155.
- [15] J. Xuan, M.K.H. Leung, D.Y.C. Leung, M. Ni, *Renew. Sust. Energy Rev.* 13 (2009) 1301–1313.
- [16] M. Sudiro, A. Bertucco, *Energy* 34 (2009) 2206–2214.
- [17] D.G. Oliva, J.A. Francesconi, M.C. Mussati, P.A. Aguirre, *Int. J. Hydrog. Energy* 35 (2010) 709–724.
- [18] F. Alcaide, G. Álvarez, J.A. Blázquez, P.L. Cabot, O. Miguel, *Int. J. Hydrog. Energy* 35 (2010) 5521–5527.
- [19] V. Liso, A.C. Olesen, M.P. Nielsen, S.K. Kaer, *Energy* 36 (2011) 4216–4226.
- [20] S. Specchia, *Catal. Today* 176 (2011) 191–196.
- [21] R. Othman, A.L. Dicks, Z. Zhu, *Int. J. Hydrog. Energy* 37 (2012) 357–372.
- [22] G. Kolb, *Chem. Eng. Process. Process Intensif.* 65 (2013) 1–44.
- [23] P. Gannon, M. Deibert, P. White, R. Smith, H. Chen, W. Priyantha, J. Lucas, V. Gorokhovskiy, *Int. J. Hydrog. Energy* 38 (2013) 431–439.
- [24] S. Specchia, V. Specchia, *Ind. Eng. Chem. Res.* 49 (2010) 6803–6809.
- [25] S. Specchia, *Int. J. Hydrog. Energy* (2014), <http://dx.doi.org/10.1016/j.ijhydene.2014.04.040>.
- [26] A.D. Ballarín, S.R. De Miguel, E.L. Jablonski, O.A. Scelza, A.A. Castro, *Catal. Today* 107 (2005) 481–486.
- [27] D.J. Moon, *Catal. Surv. Asia* 12 (2008) 88–202.
- [28] H. Er-rbib, C. Bouallou, F. Werkoff, *Energy Procedia* 29 (2012) 156–165.
- [29] S. Specchia, G. Negro, G. Saracco, V. Specchia, *Appl. Catal. B: Environ.* 70 (2007) 525–531.
- [30] L.D. Vella, J.A. Villoria, S. Specchia, N. Mota, J.L.G. Fierro, V. Specchia, *Catal. Today* 171 (2011) 84–96.
- [31] L.D. Vella, S. Specchia, *Catal. Today* 176 (2011) 340–346.
- [32] L. Pino, A. Vita, M. Cordaro, V. Recupero, M.S. Hegde, *Appl. Catal. A: Gen.* 243 (2003) 135–146.
- [33] T. Rampe, A. Heinzl, B. Vogel, *J. Power Sources* 86 (2000) 536–541.
- [34] A. Cuttillo, S. Specchia, M. Antonini, G. Saracco, V. Specchia, *J. Power Sources* 154 (2006) 379–385.
- [35] H. Mei, C. Li, S. Ji, H. Liu, *Chem. Eng. Sci.* 62 (2007) 4294–4303.
- [36] M. O’Connell, G. Kolb, K.P. Schelhaas, J. Schürer, D. Tiemann, A. Ziogas, V. Hessel, *Int. J. Hydrog. Energy* 34 (2009) 6290–6303.
- [37] N.R. Peela, D. Kunzru, *Int. J. Hydrog. Energy* 36 (2011) 3384–3396.
- [38] J.A. Villoria, M.C. Alvarez-Galvan, S.M. Al-Zahrani, P. Palmisano, S. Specchia, V. Specchia, J.G.L. Fierro, R.M. Navarro, *Appl. Catal. B: Environ.* 105 (2011) 276–288.
- [39] T. Leandro de Souza, C. de Cássia Rodrigues da Silva Rossi, C. Gonçalves Alonso, R. Guirardello, V. Ferreira Cabral, N.R. Camargo Fernandes-Machado, S. Specchia, M. Santiago Zabalyo, L. Cardozo-Filho, *Int. J. Hydrog. Energy* 39 (2014) 8257–8270.
- [40] M.H. Akbari, A.H. Sharafian Ardakani, M. Andisheh Tadbir, *Chem. Eng. J.* 166 (2011) 1116–1125.
- [41] M. Krumpelt, T.R. Krause, J.D. Carter, J.P. Kopasz, S. Ahmed, *Catal. Today* 77 (2002) 3–16.
- [42] J.R. Rostrup-Nielsen, *Phys. Chem. Chem. Phys.* 3 (2001) 283–288.
- [43] F. Joensen, J.R. Rostrup-Nielsen, *J. Power Sources* 105 (2002) 195–201.
- [44] G. Gonçalves, M.K. Lenzi, O.A.A. Santos, L.M.M. Jorge, *J. Non-Cryst. Solids* 352 (2006) 3697–3704.
- [45] J. Sehested, *Catal. Today* 111 (2006) 103–110.
- [46] J.G. Seo, M.H. Youn, J.C. Jung, I.K. Song, *Int. J. Hydrog. Energy* 35 (2010) 6738–6746.
- [47] J.-H. Kim, D.J. Suh, T.-J. Park, K.-L. Kim, *Appl. Catal. A: Gen.* 197 (2000) 191–200.
- [48] M.L. Toebes, J.H. Bitter, A. Jos van Dillen, K.P. De Jong, *Catal. Today* 76 (2002) 33–42.
- [49] J.R. Rostrup-Nielsen, in: J.R. Anderson, M. Boudart (Eds.), *Catalysis: Science and Technology*, 5, Springer Verlag, New York, 1984, pp. 1–117.
- [50] L. Pino, A. Vita, F. Cipiti, M. Laganà, V. Recupero, *Appl. Catal. A: Gen.* 306 (2006) 68–77.
- [51] M.C. Alvarez-Galvan, R. Navarro, F. Rosa, Y. Briceno, F.G. Alvarez, J.L.G. Fierro, *Int. J. Hydrog. Energy* 33 (2008) 652–663.
- [52] L.S. Carvalho, A.R. Martins, P. Reyes, M. Oportus, A. Albonoz, V. Vicentini, M. Do Carmo Rangel, *Catal. Today* 142 (2009) 52–60.
- [53] B. Nematollahi, M. Rezaei, M. Khajenoori, *Int. J. Hydrog. Energy* 36 (2011) 2969–2978.
- [54] C. Fauteux-Lefebvre, N. Abatzoglou, N. Braid, I.E. Achouri, *J. Power Sources* 196 (2011) 7673–7680.
- [55] K. Kusakabe, K.I. Sotowa, T. Eda, Y. Iwamoto, *Fuel Process. Technol.* 86 (2004) 319–326.
- [56] M. El Doukali, A. Iriondo, P.L. Arias, J.F. Cambra, I. Gandarias, V.L. Barrio, *Int. J. Hydrog. Energy* 37 (2012) 8298–8309.
- [57] P. Fornasiero, R. Di Monte, T. Montini, J. Kašpar, M. Graziani, *Stud. Surf. Sci. Catal.* 130 (2000) 1355–1360.
- [58] R. Craciun, W. Daniell, H. Knözinger, *Appl. Catal. A: Gen.* 230 (2002) 153–168.
- [59] R. Wang, H. Xu, X. Liu, Q. Ge, W. Li, *Appl. Catal. A: Gen.* 305 (2006) 204–210.
- [60] L.S.F. Feio, C.E. Hori, S. Damyanova, F.B. Noronha, W.H. Cassinelli, C.M.P. Marques, J.M.C. Bueno, *Appl. Catal. A: Gen.* 316 (2007) 107–116.
- [61] B.T. Schädel, M. Duisberg, O. Deutschmann, *Catal. Today* 142 (2009) 42–51.
- [62] M.H. Halabi, M.H.J.M. De Croon, J. Van der Schaaf, P.D. Cobden, J.C. Schouten, *Appl. Catal. A: Gen.* 389 (2010) 68–79.
- [63] U. Amjad, A. Vita, C. Galletti, L. Pino, S. Specchia, *Ind. Eng. Chem. Res.* 52 (2013) 15428–15436.
- [64] W. Shan, M. Luo, P. Ying, W. Shen, C. Li, *Appl. Catal. A: Gen.* 246 (2003) 1–9.
- [65] S. Hosokawa, M. Taniguchi, K. Utani, H. Kanai, S. Imamura, *Appl. Catal. A: Gen.* 289 (2005) 115–120.
- [66] L. Pino, A. Vita, F. Cipiti, M. Laganà, V. Recupero, *Catal. Lett.* 122 (2008) 121–130.
- [67] L. Pino, A. Vita, F. Cipiti, M. Laganà, V. Recupero, *Appl. Catal. B: Environ.* 104 (2011) 64–73.
- [68] G. Kolb, T. Baier, J. Schürer, D. Tiemann, A. Ziogas, H. Ehwald, *Chem. Eng. J.* 137 (2008) 653–663.
- [69] G.D. Stefanidis, D.G. Vlachos, *Chem. Eng. Sci.* 65 (2010) 398–404.
- [70] G. Kolb, T. Baier, J. Schürer, D. Tiemann, A. Ziogas, S. Specchia, C. Galletti, G. Germani, Y. Schuurman, *Chem. Eng. J.* 138 (2008) 474–489.
- [71] F. Haghighi Bijan, *Int. J. Hydrog. Energy* 28 (2003) 1369–1377.
- [72] A.R. Tadd, B.D. Gould, J.W. Schwank, *Catal. Today* 110 (2005) 68–75.
- [73] I. Aartun, H. Venvik, A. Holmen, P. Pfeifer, O. Görke, K. Schubert, *Catal. Today* 110 (2005) 98–107.
- [74] J.M. Bae, S. Ahmed, R. Kumar, E. Doss, *J. Power Sources* 139 (2005) 91–95.
- [75] A. Qi, S. Wang, C. Ni, D. Wu, *Int. J. Hydrog. Energy* 32 (2007) 981–991.
- [76] B. Lindström, J.A.J. Karlsson, P. Ekdunge, L. De Verdier, B. Häggendal, J. Dawody, M. Nilsson, L.J. Pettersson, *Int. J. Hydrog. Energy* 34 (2009) 3367–3381.
- [77] A. Vita, L. Pino, F. Cipiti, M. Laganà, V. Recupero, *Int. J. Hydrog. Energy* 35 (2010) 9810–9817.
- [78] O. Sanz, F.J. Echave, F. Romero-Sarria, J.A. Odriozola, M. Montes, in: L.M. Gandia, G. Arzamendi, P.M. Dieguez (Eds.), *Renewable Hydrogen Technologies: Production, Purification, Storage, Applications and Safety*, Elsevier B.V., Amsterdam, 2013, pp. 201–224.
- [79] E.D. Banús, V.G. Milt, E.E. Miró, M.A. Ulla, *Appl. Catal. B: Environ.* 132–133 (2013) 479–486.
- [80] P. Avila, M. Montes, E.E. Miró, *Chem. Eng. J.* 109 (2005) 11–36.
- [81] S. Specchia, C. Galletti, V. Specchia, *Stud. Surf. Sci. Catal.* 175 (2010) 59–67.
- [82] S. Specchia, E. Finocchio, G. Busca, V. Specchia, in: M. Lackner, F. Winter, A.K. Agarwal (Eds.), *Handbook of Combustion*, Wiley-VCH Verlag GmbH & Co. KGaA, Weinheim, 2011, pp. 439–472.
- [83] S.L. González-Cortés, F.E. Imbert, *Appl. Catal. A: Gen.* 452 (2013) 117–131.
- [84] A. Vita, G. Cristiano, C. Italiano, S. Specchia, F. Cipiti, V. Specchia, *Int. J. Hydrog. Energy* (2014), <http://dx.doi.org/10.1016/j.ijhydene.2014.03.114>.
- [85] A. Cybulski, J.A. Moulijn, *Catal. Rev. Sci. Eng.* 36 (1994) 179–270.
- [86] F.C. Patcas, G.I. Garrido, B. Kraushaar-Czarnetzki, *Chem. Eng. Sci.* 62 (2007) 3984–3990.
- [87] M. Valentini, G. Groppi, C. Cristiani, M. Levi, E. Tronconi, P. Forzatti, *Catal. Today* 69 (2001) 307–314.
- [88] N. Laosiripojana, S. Assabumrungrat, *Chem. Eng. Sci.* 61 (2006) 2540–2549.
- [89] C. Diagne, H. Idriss, A. Kiennemann, *Catal. Commun.* 3 (2002) 565–571.
- [90] L. Zhu, J.-Q. Lu, P. Chen, X. Hong, G.-Q. Xie, G.-S. Hu, M.-F. Luo, *J. Mol. Catal. A: Chem.* 361–362 (2012) 52–57.
- [91] Y. Mukainakano, B. Li, S. Kado, T. Miyazawa, K. Okumura, T. Miyao, S. Naito, K. Kunimori, K. Tomishige, *Appl. Catal. A: Gen.* 318 (2007) 252–264.
- [92] D. Dissanayake, M.P. Rosynek, K.C. Kharas, J.H. Lunsford, *J. Catal.* 132 (1991) 117–127.
- [93] D. Ugues, S. Specchia, G. Saracco, *Ind. Eng. Chem. Res.* 43 (2004) 1990–1998.
- [94] S.L. González-Cortés, F.E. Imbert, *Appl. Catal. A: Gen.* 452 (2013) 117–131.

- [95] G. Groppi, A. Beretta, E. Tronconi, in: A. Cybulski, J.A. Moulijn (Eds.), *Structured Catalysts and Reactors*, CRC Press, Taylor & Francis Group, Boca Raton, 2006, pp. 243–310.
- [96] R.J. Farrauto, *Chem. Eng. J.* 238 (2014) 172–177.
- [97] G. Jones, J.G. Jakobsen, S.S. Shim, J. Kleis, M.P. Andersson, J. Rossmeyl, F. Abild-Pedersen, T. Bligaard, S. Helveg, B. Hinnemann, J.R. Rostrup-Nielsen, I. Chorkendorff, J. Sehested, J.K. Nørskov, *J. Catal.* 259 (2008) 147–160.
- [98] S. Ayabe, H. Omoto, T. Utaka, R. Kikuchi, K. Sasaki, Y. Teraoka, K. Eguchi, *Appl. Catal. A: Gen.* 241 (2003) 261–269.
- [99] D.E. Mears, *J. Catal.* 30 (1973) 283–287.
- [100] G. Kolb, V. Hessel, *Chem. Eng. J.* 98 (2004) 1–38.
- [101] G. Kolb, R. Zapf, V. Hessel, H. Löwe, *Appl. Catal. A: Gen.* 277 (2004) 155–166.
- [102] V. Specchia, G. Baldi, S. Sicardi, *Chem. Eng. Commun.* 4 (1980) 361–380.
- [103] B. Li, K. Maruyama, M. Nurunnabi, K. Kunimori, K. Tomishige, *Appl. Catal. B: Environ.* 275 (2004) 157–172.
- [104] J.H. Kim, D.J. Suh, T.J. Park, K.L. Kim, *Appl. Catal. A: Gen.* 197 (2000) 191–200.
- [105] V.C.H. Kroll, H.M. Swann, C. Mirodatos, *J. Catal.* 161 (1996) 409–422.